Journal of Power Sources 196 (2011) 3015–3025

Contents lists available at ScienceDirect

Journal of Power Sources

journal homepage: www.elsevier.com/locate/jpowsour

Design and fabrication of a silicon-based direct methanol fuel cell with a new cathode spoke structure

Yufeng Zhang[a,b,*], Zhenyu Yuan[a], Yuling Li[a], Qi Jia[a], Song Chen[a], Xiaowei Liu[a,b]

[a] MEMS Center, Harbin Institute of Technology, Harbin 150001, China
[b] Key Laboratory of Micro-systems and Micro-structures Manufacturing, Ministry of Education, Harbin 150001, China

ARTICLE INFO

Article history:
Received 6 October 2010
Received in revised form
18 November 2010
Accepted 22 November 2010
Available online 26 November 2010

Keywords:
Micro direct methanol fuel cell
Self-breathing
Cathode structure
Spoke

ABSTRACT

In this paper, a self-breathing micro direct methanol fuel cell (μDMFC) featuring a new cathode current collector with a spoke configuration is presented to improve cell performance. Simulation results show that the new spoke structure can effectively increase the efficiency of oxygen mass transport and exhibit higher pressure than the conventional perforated structure. The water transfer to the proton exchange membrane (PEM) is promoted to reduce the PEM resistance with the increase in the membrane water content. Additionally, the effects of the spoke blades on performance were evaluated to determine the optimal cathode structure. The self-breathing μDMFCs with conventional and new cathode structures were fabricated using silicon-based micro-electromechanical system (MEMS) technologies and tested at room temperature with 1 M methanol solution. The experimental results revealed that the spoke cathode structure exhibits significantly higher performance than the conventional structure, showing a substantial 30% increase in peak power density.

1. Introduction

Fuel cells are ideal candidates for portable applications due to their high efficiency, simplicity, low emissions and silence, but their drawback currently is their high cost. Compared with other fuel cell types, the direct methanol fuel cell (DMFC) has the advantages of a low operating temperature (below 100 °C), a fast response to dynamic loads and quick start-up. Thus, a DMFC may potentially replace and/or assist batteries in portable electrical appliances as the best candidate for a power sources. With the development of micro-electromechanical system (MEMS) technologies, micro direct methanol fuel cells (μDMFC) have been a breakthrough for micro power sources, which are appropriate to apply in a 3C device (computer, communication, and consumer electronics) and in personal portable system in the future [1–7]. In consideration of the potential of μDMFCs to replace conventional power sources, many researchers have paid increasing attention to various aspects of μDMFC technology [8–11]. The cathode self-breathing configuration without an auxiliary oxygen-driven device to consume power is a crucial factor for the portable applications [12,13]. During operation, oxygen from the air accesses the cathode by convection and diffusion for the electrochemical reaction. Compared with a gas fan or oxygen tank to supply the oxidant, a self-breathing mode yields a low feeding speed, resulting in the deterioration of the electrochemical reaction, which negatively affects achievement of the best performance of the μDMFCs [14,15].

Presently, the study of the cathode self-breathing structures has mainly focused on the parameter optimizations and new configuration designs. Chen et al. [16] presented a two-dimensional, two-phase thermal model for direct methanol fuel cells in which the fuel and oxidant are fed in a passive manner. The model coupled heat and mass transport, as well as the electrochemical reactions. They investigated the effects of various operating and geometric design parameters, including methanol concentration as well as the open ratio and channel and rib width of the current collectors on cell performance. Hwang [17] developed a three-dimensional numerical model to study the electrochemical species characteristics in a perforated cathode. The radius of the perforated cathode was varied to examine its effect on the electrochemical performance. Kim [14] employed a cathode structure with various hole shapes and opening ratios to evaluate the effects of the cathode on cell performance. He indicated that a rectangular cathode opening pattern with a 65% opening ratio and a circular cathode hole pattern with a 38% opening ratio gave the highest performance, while a lower opening ratio of the circular cathode hole pattern caused cathode flooding and resulted in an unstable output. Guo [18] designed a fuel cell with a window-frame cathode structure, which provided a large open area for more efficient mass transfer, and the peak power outputs achieved was 519.0 mW with active areas of 18.0 cm^2. Oliveira et al. [19] experimentally investigated the effects of three different anode and cathode flow field designs

* Corresponding author at: MEMS Center, Harbin Institute of Technology, Harbin 150001, China. Tel.: +86 451 86413451; fax: +86 451 86413441.
E-mail address: yufeng_zhang@hit.edu.cn (Y. Zhang).

0378-7753/$ – see front matter © 2010 Elsevier B.V. All rights reserved.
doi:10.1016/j.jpowsour.2010.11.111

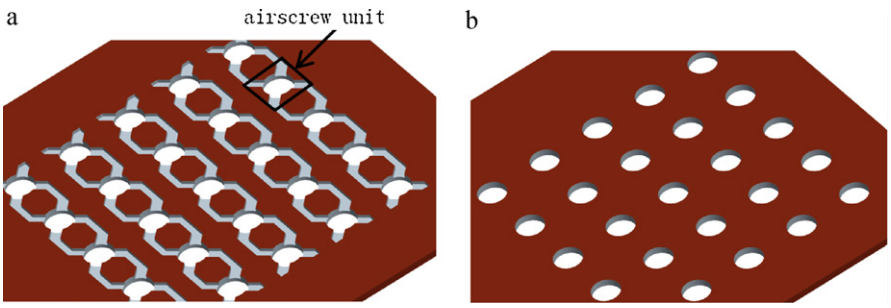

Fig. 1. Schematic of the air-breathing cathode with the spoke structure.

consisting of a single serpentine (SFF), a multi-serpentine (MSFF) and an original design mixed parallel and serpentine (MFF) on the performance of a DMFC. Their work showed that the MSFF as a cathode structure had a positive effect on the cell voltage and power at ambient temperature, while the use of the SFF had a better performance at a high cell temperature. Jung et al. [20] studied the effects of the different cathode structures, serpentine, parallel and grid, on cell performance and found that the DMFCs with the serpentine structure performed the best and had the highest stability due to their better mass transport and reactant distribution.

At present, some efforts have been made to investigate the cathode opening ratios and shapes for self-breathing DMFCs [15]. Most studies report that the conventional cathode perforated-plate structure is widely applied in self-breathing DMFCs, as shown in Fig. 1(a), but the best opening ratio differs according to the shapes of the holes. However, two factors have a great effect on the performance of the self-breathing μDMFCs with the cathode perforated structure. First, the mass transport efficiency of the oxidant on the gas diffusion layer is slow and inhomogeneous. Second, water flooding on the cathode prevents the oxidant mass transport. Therefore, the cathode structure significantly influences the self-breathing μDMFC performance because of its effects on the ohmic and mass transport loss. However, few efforts have been made to optimize the cathode structure, which is critical.

To ensure that the oxygen from air can enter the electrochemical reaction sufficiently and is well-distributed, this study intended to design a self-breathing μDMFC with a new cathode spoke structure, as illustrated in Fig. 1(b). With a back interface (air-contacting interface) structure similar to a conventional perforated cathode, its front interface (electrode-contacting interface) is equipped with a certain number of blade-form channels, which are connected with self-breathing circular openings to form a "spoke" unit. These units are connected via extended channels to form a dual-loop airflow. During its operation, air from the circular openings in the back interface is distributed around the MEA and is deoxidized. Compared with a conventional perforated cathode, the spoke cathode has an enlarged interface between the oxidant and diffusion layer with the same open ratios, thereby making oxygen enter the electrochemical reaction in a more sufficient and uniform way. Moreover, the self-breathing μDMFCs with the different cathode structures are fabricated on the silicon substrates utilizing MEMS technologies, and an optimized assembly that can ensure the tightness in the encapsulation process is also discussed in this paper.

2. Model and simulation

2.1. Model description and assumption

Two factors make the performance of a self-breathing μDMFC less efficient than that of an active oxygen-feeding μDMFC. Firstly, the speed of oxidant mass transport in the diffusion layer is low and non-uniform. This negatively impacts the process and efficiency of the electrochemical reaction. Secondly, the water-flooding caused by the low efficiency of discharging water generated in the cathode negatively influences the oxygen mass transport. Therefore, efforts to design the self-breathing cathode structure will contribute to improving the cell performance. Thus, we present a new cathode self-breathing spoke structure to ensure that the oxygen from the air can enter the electrochemical reaction sufficiently and is well distributed.

To validate the spoke structure effectively, we built a three-dimensional two-phase flow model for self-breathing μDMFCs to investigate the mass transport and reaction principle based on a two-phase thermal model for passive DMFC in a former work [16]. The N–S equation was applied to describe gas flow in the cathode channel. For simplification, the domain simulated is a typical unit of a μDMFC cathode in the form of a perforated and spoke cathode with area of 1.2 mm × 1.2 mm, as shown in Fig. 2, including the PEM, catalyst layer, diffusion layer and gas flow channel. The thicknesses of the PEM and catalyst layer are both 75 μm. The catalyst layer is simplified as a plane with a thickness of zero. The height of the gas flow channel and diameter of the holes in the back interface are 210 μm and 800 μm, respectively, and the spoke structures have a different number of blades (2, 4 and 8). The height and radial length of the blades are 100 μm and 848.4 μm, respectively. Several assumptions for simplification are introduced in this model:

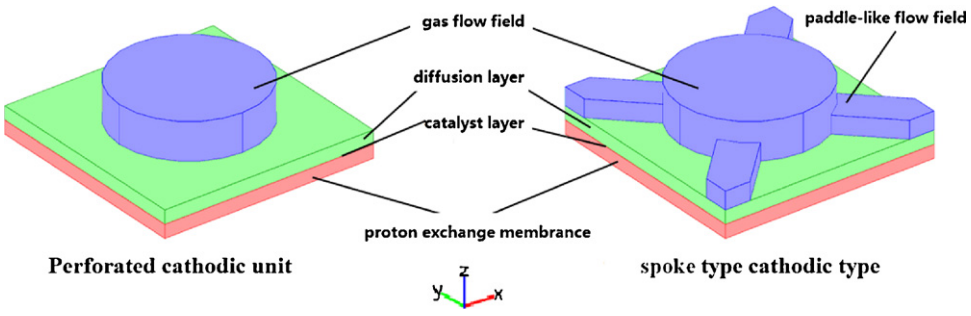

Fig. 2. Schematic of simulation domains of the three-dimensional model for the μDMFC cathode.

(1) All processes in the μDMFC are under steady-state conditions.
(2) All gases are considered to be uncompressible and ideal gases.
(3) The flow of the gases is considered to be laminar flow because of a low Reynolds number.
(4) The proton exchange membrane and diffusion layer are assumed to be a homogeneous porous electrodes (Table 1).

2.2. Governing equations

In the three-dimensional model, the electrical potential variations along the direction vertical to the diffusion layer are described by the conductive media DC equation. The distribution of oxygen, water in the air and nitrogen in the flow channel and diffusion layer is described by the Maxwell–Stefan diffusion and convection equation, with mass fraction as the variable. The description of the speed and pressure of the gas in the diffusion layer is based on Darcy's law. In the flow channel, the incompressible Navier–Stokes equation is utilized to describe the air flow and changes in the pressure. The temperature distribution in cathode is studied with the heat generated in the catalyst surface layer, and that from conductance and the flow channel.

The transport of the electrons and protons are controlled by the solid-phase electronic potential and the membrane ionic potential, respectively. As the overlay region of the solid and electrolyte, the catalyst layer provides the reaction channel for the electrons, protons and related reaction molecules, which enhances the successful reaction. Clearly, the electronic current flows in the diffusion layer and catalyst layer, while the ionic current resides in the catalyst layer and PEM [17].

There is no electrochemical reaction in the diffusion layer, and the source term of the electronic current is set to zero and expressed as follows:

$$-\nabla(-\sigma_s \nabla\phi_s) = 0, \tag{1}$$

where σ_s is the electronic conductivity ($S\,m^{-1}$), and ϕ_3 is the potential in the catalyst layer (V). Similarly, the source term for the ionic current in the PEM should be zero.

$$-\nabla(-\sigma_l \nabla\phi_l) = 0, \tag{2}$$

where σ_l is conductivity of the free electrolyte ($S\,m^{-1}$), and ϕ_3 is the electrolyte potential (V). The ionic balance and electron balance in the catalyst layer, the region where the reaction happens, are described as follows:

$$-\nabla(-\sigma_{l,\mathrm{eff}} \nabla\phi_l) = -S_a i_c \tag{3}$$

$$-\nabla(-\sigma_{s,\mathrm{eff}} \nabla\phi_s) = S_a i_c \tag{4}$$

where $\sigma_{s,\mathrm{eff}}$ and $\sigma_{l,\mathrm{eff}}$ are the solid-phase effective electronic conductivity ($S\,m^{-1}$) and the electrolyte effective conductivity ($S\,m^{-1}$), respectively. S_a represents the surface area (m^{-1}), and i_c is the current density ($A\,m^{-2}$).

The multi-component mixed gas diffusion is governed by the equation:

$$n_i = \left\{ -\rho_g w_i \sum_{j=1}^{3} \frac{M D_{ij}}{M_j} \left(\nabla w_j + \frac{w_j}{M} \nabla M \right) + w_i \rho_g u_{\boldsymbol{g}} \right\}, \tag{5}$$

where n_i represents the mass fluxes for all components, ρ_g is the mixed gas density, w_i is the mass fraction of the component i, M is the molar mass of the mixed gas, D_{ij} describes the gas i's molecular diffusion coefficient with the component j, and u_g represents the gas velocity.

The diffusion of the oxygen concentration is described by the convection–diffusion equation:

$$\nabla \cdot (-D \nabla c_{\mathrm{O_2}}) = R - \boldsymbol{u_g} \cdot \nabla c_{\mathrm{O_2}}, \tag{6}$$

where D is the one-dimensional diffusion coefficient, and $c_{\mathrm{O_2}}$ is the oxygen concentration.

The force caused by the attractive forces between liquid-phase molecules is called surface tension. In the porous media, the surface tension causes the motion of the vapor–liquid two-phase species, impels the two-phase interface to move and redistributes the velocity and concentration for the different species. In this mathematical model, the pressure difference p_c caused by the surface tension becomes the transport power for the water formed in the cathode.

$$p_c = p_g - p_l = \sigma \cos(\theta_c) \left(\frac{\varepsilon}{K} \right)^{0.5} J(s), \tag{7}$$

where p_g is the pressure of the gas phase, p_l is the pressure of the liquid phase, σ represents the surface tension coefficient, θ_c is the contact angle, ε is the porosity in the porous media, $J(s)$ represents the Leverette function, and s represents the liquid saturation in a porous medium.

In a porous medium surface, there are two forms for the liquid-phase, a spreading state and a shrinking state, which depend on the differential wetting of the porous materials. The contact angle θ_c is a quantitative measure of the wetting of a solid by a liquid. It is the angle formed by the liquid at the three phase boundary where a liquid, gas and solid intersect. If the contact angle is less than 90°, the porous medium is hydrophilic and the value of the surface tension is positive. If the contact angle is greater than 90°, the porous medium should be hydrophobic and the value of the surface tension is negative. $J(s)$ is expressed as follows:

$$J(s) = \begin{cases} 1.417(1-s) - 2.120(1-s)^2 + 1.263(1-s)^3 & 0 < \theta_c < 90^\circ \\ 1.417s - 2.120s^2 + 1.263s^3 & 90^\circ < \theta_c < 180^\circ \end{cases} \tag{8}$$

The mass transport equation for liquid water is as follows:

$$-\nabla \cdot \left(\frac{\rho_l}{M_l} \boldsymbol{u_l} \right) + R_w = 0, \tag{9}$$

where ρ_l and M_l are the water density and molar mass, respectively, R_w stands for the water transfer rate between the two phases and $\boldsymbol{u_l}$ is the velocity of the water in the porous medium which is described by Darcy's law:

$$\boldsymbol{u_l} = -\frac{K k_{rl}}{\mu_l} \nabla p_l, \tag{10}$$

where K represents the absolute permeability of the porous medium, $\boldsymbol{\mu_l}$ is the dynamic viscosity of the liquid-phase, k_{r1} is the relative permeability of the liquid-phase and is related to the liquid saturation. In a porous medium, the gas-phase shares space with the liquid-phase, reducing the effective motion space of the liquid-phase and affecting the velocity of the liquid-phase. k_{r1} is the correction coefficient of the liquid-phase velocity, shown as follows:

$$k_{rl} = s^3 \tag{11}$$

With the above analysis, combining Eqs. (7), (9) and (10) yields the mass transport equation of the liquid-phase:

$$-\nabla \cdot \left(-\frac{\rho_l}{M_l} \frac{K k_{rl}}{\mu_l} \sigma \cos(\theta_c) \left(\frac{\varepsilon}{K} \right)^{0.5} \nabla J(s) \right) + R_w = 0. \tag{12}$$

The gas flow in the cathode flow channel is expressed by the N–S equation:

$$\rho_g \frac{\partial \boldsymbol{u_g}}{\partial t} - \nabla \cdot \mu_g (\nabla \boldsymbol{u_g} + (\nabla \boldsymbol{u_g})^T) + \rho_g (\boldsymbol{u_g} \cdot \nabla) \boldsymbol{u_g} + \nabla p_c = 0, \tag{13}$$

where $\boldsymbol{\mu_g}$ represents the gas-phase viscosity coefficient, and p_c represents the pressure in the flow channel.

The gas velocity in the diffusion layer can be written as:

$$\boldsymbol{u_g} = -\frac{K k_{rg}}{\mu_g} \nabla p_g, \tag{14}$$

where k_{rg} is the relative permeability of the gas-phase.

$$k_{rg} = (1-s)^3 \tag{15}$$

For the sake of simplicity, the following simplified Butler–Volmer equation is used for explaining the relationship between the current and potential:

$$i_c = i_0 \left(\frac{c_{O_2}}{c_{O_2,\mathrm{ref}}} \right) \exp\left(-\frac{\alpha_c F(\phi_S - \phi_l)}{RT_0} \right) \tag{16}$$

where i_0 represents the reference cathode exchange current density, c_{O_2} represents the oxygen concentration, $c_{O_2,\mathrm{ref}}$ is the reference concentration of oxygen, α_c is the transfer coefficient at the anode, R is for the universal gas law constant, F is the Faraday constant, and T_0 is the temperature.

According to the first law of thermodynamics, we obtain the conservation equation of energy considering the effect of porosity:

$$\nabla \cdot (-k\nabla T_1) = Q - \rho_g C_p \boldsymbol{u_g} \nabla T_1, \tag{17}$$

where k is the thermal conductivity of the porous medium, C_p represents the specific heat at a constant pressure, and Q represents the energy source term of the fluid.

$$Q = i_c(\phi_S - \phi_l) - i_c \frac{\Delta H_c - \Delta G_c}{nF} - h_v N_{H_2O}, \tag{18}$$

where i_c is the cathode current density, ΔH_c is the cathode reaction enthalpy, ΔG_c is the Gibbs free energy, h_v is the latent heat of water, and N_{H_2O} is the flux of the vapor.

For the above equation, the first term shows that the heat due to activation is overpotential on the cathode, the second term accounts for the entropic loss, and the last term reflects the heat caused by the evaporation of liquid water.

2.3. Boundary conditions

At the inlet of the flow channel, the oxygen concentration is set as:

$$C_{O_2} = C_{O_2,\mathrm{in}}, \tag{19}$$

and the gas-phase pressure is:

$$p_g = p_{\mathrm{atm}}, \tag{20}$$

The temperature distribution obeys the natural convection principle. At the interface of the flow channel and the diffusion layer, Darcy's law is simplified as:

$$\boldsymbol{u_g} = \frac{K}{\mu_g}(p_{\mathrm{atm}} - p). \tag{21}$$

The liquid saturation is assumed to be 0.05, and the potential on this interface is equal to 0.7 V.

$$s = 0.05 \tag{22}$$

$$\phi_s = 0.7\mathrm{V} \tag{23}$$

The temperature is continuous on this interface.

At the surface between the diffusion layer and the catalyst layer, the flux of water is described as:

$$N_{H_2O} = \frac{i_c}{2F} + n_d \frac{i_c}{F}. \tag{24}$$

The boundary condition for the oxygen mass transport is as follows:

$$N_{O_2} = -\frac{i_c}{4F}. \tag{25}$$

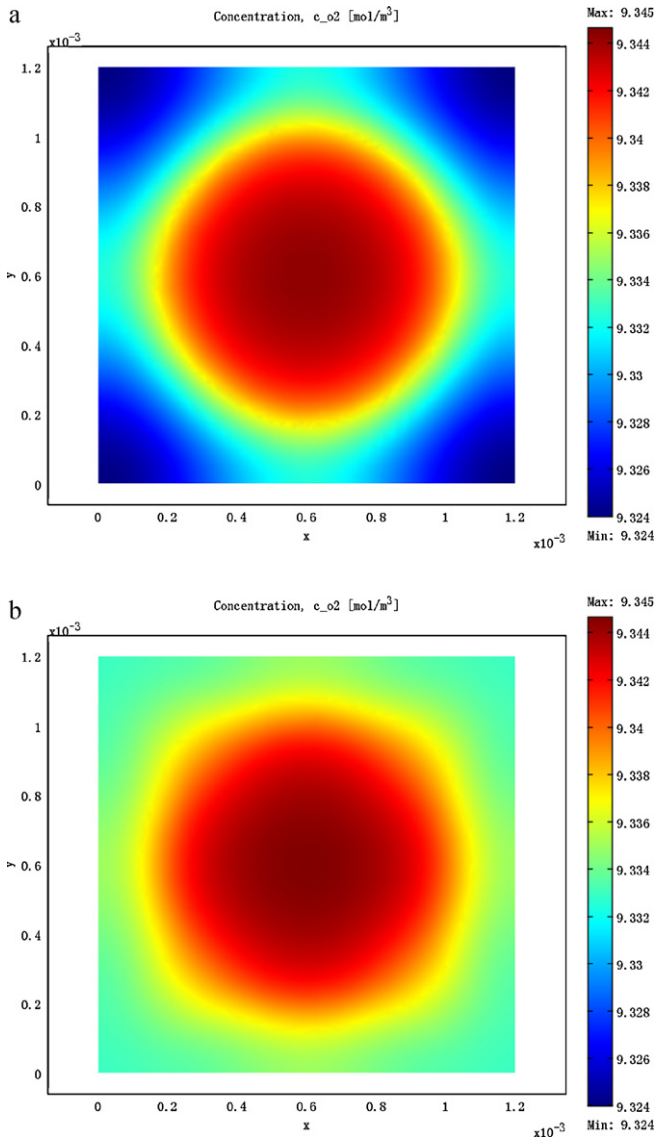

Fig. 3. Oxygen concentration distributions at the catalyst layers with different cathode structures (mol m^{-3}): (a) perforated cathode and (b) spoke cathode.

From the Darcy's law, the $\boldsymbol{u_g}$ should be:

$$\boldsymbol{u_g} = -N_{O_2} \cdot \frac{M_{O_2}}{\rho_{O_2}}. \tag{26}$$

Because of the electrochemical reaction, the electron and proton transfer balances are expressed as:

$$n \cdot (\sigma \nabla \phi_s) = i \tag{27}$$

$$n \cdot (\sigma \nabla \phi_m) = -i. \tag{28}$$

The flux for the oxygen is:

$$N_{O_2} = -\frac{i_c}{4F}. \tag{29}$$

2.4. Analysis of model results

The coupled equations were numerically solved by the finite element method using COMSOL Multiphysics 3.5. Computation was performed on 7076 unstructured meshes. A grid-independence test was executed by two additional fine and extra fine meshes. The calculation time was about 254.27 s on a Pentium(R) E2180 2.00-GHz PC.

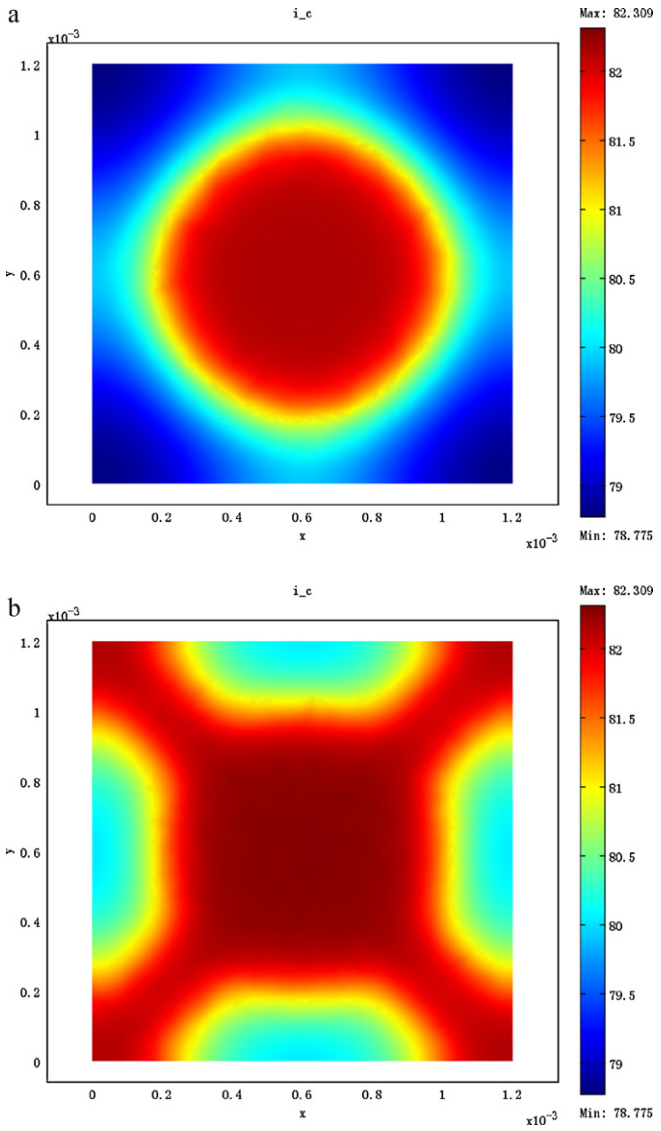

Fig. 4. Current density distributions at the catalyst layers with different cathode structures (A m^{-2}): (a) perforated cathode and (b) spoke cathode.

Based on the three-dimensional model, we analyzed the impact of the cathode structure, the perforated and four-blade spoke cathode (the blade width was 200 μm), shown in Fig. 2, on the component delivery and reaction principle within the cell. Fig. 3 shows the oxygen concentration distribution on the surface of the catalyst layer. With the same initial value, the minimum oxygen concentration of the spoke cathode was 9.333 mol m^{-3}, while that of the perforated cathode was 9.324 mol m^{-3}. We determined that the structure of the spoke cathode effectively increased the efficiency of oxygen mass transport among the electrodes, leading to a concentration gap of the oxidant on the surface of the catalyst layer. For the μDMFC, such a slight gap could has a marked impact on its performance. Furthermore, the blades make the concentrations more equal. There are no dead angles for the mass transport appearing in Fig. 3. This ensures a sufficient supply of the oxidant and effectively avoids concentration polarization.

Fig. 4 shows the current density distribution on the surface of the catalyst layer of the perforated and spoke cathode. With a fixed cathode overpotential, the latter showed an average higher density than the former. This is attributable to the high oxygen concentration that the spoke cathode has, which led to a more sufficient

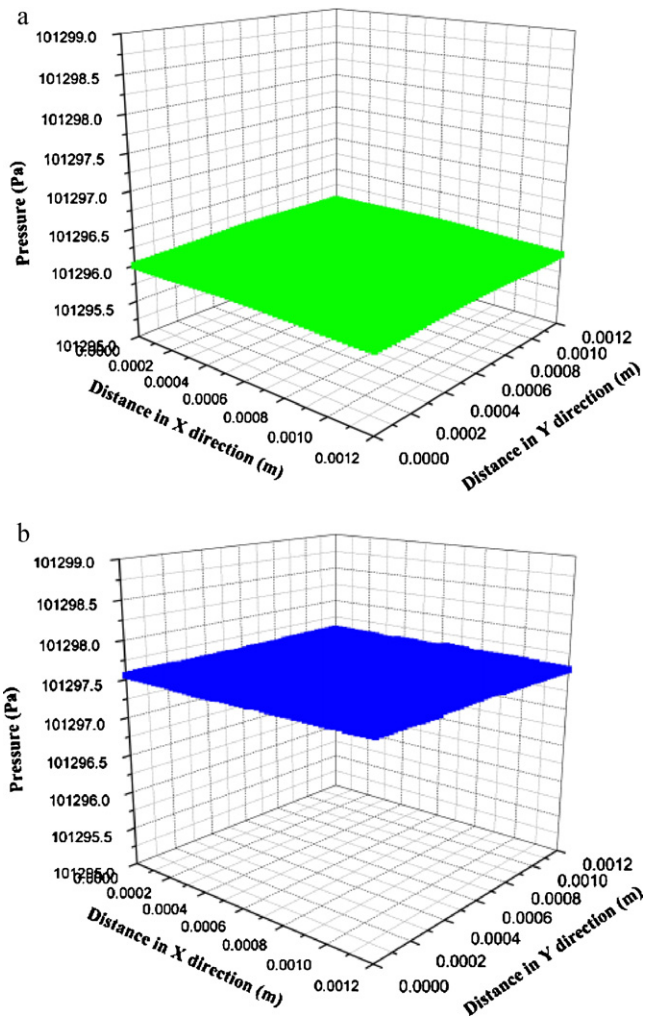

Fig. 5. Pressure distribution in the surface of catalyst layer with different cathode structures (Pa): (a) perforated cathode and (b) spoke cathode.

reaction than the other. Therefore, the spoke cathode appeared to have an advantage in promoting reaction speed on the surface, giving rise to a high performance.

Fig. 5 shows a comparison of the pressure distribution on the surface of the catalyst layer for the two cathode structures. The average pressure of the spoke cathode, at approximately 101.2975 kPa, was higher than that of the perforated cathode (~101.096 kPa). In addition to preventing methanol penetration from the anode to the cathode, the increasing pressure also promoted the water transfer to the PEM and thereby also promoted the rising membrane water content and the declining inner resistance among the PEM.

The temperature distribution is shown in Fig. 6. Clearly, the temperature of the spoke cathode was higher than that of the perforated cathode. This is due to the higher reaction speed of the former. The interior temperature distribution has a significant impact on the cell performance. An increasing temperature has the following advantages: (1) enchancing the electrocatalytic activity of the catalyst, (2) increasing the diffusion rate of oxygen, (3) promoting the air vaporization in the cathode, and thus alleviating the problem of water-flooding, and (4) increasing the diffusion rate of the water from the catalyst electrode to the PEM, thereby promoting protontran transport, and increasing power efficiency.

While the temperature of the spoke cathode is relatively high, there is only a small gap of 0.0947 K, which is lower than the

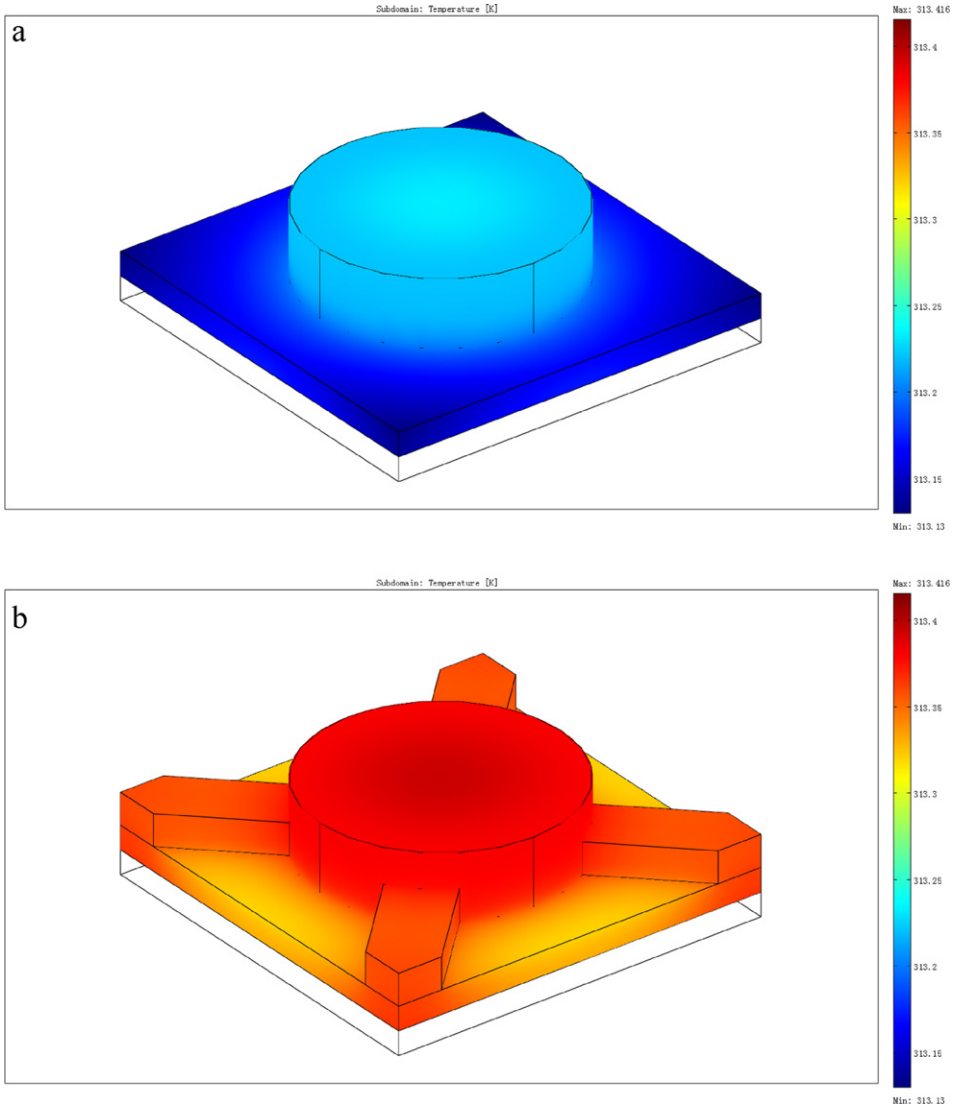

Fig. 6. Internal temperature distributions with different cathode structures (K): (a) perforated cathode and (b) spoke cathode.

0.1226 K of the perforated cathode. This means that the former possessed a more uniform distribution. Despite the small size of this gap for a single unit, the overall gap was markedly larger as the cell was composed of a number of such units. This makes the spoke cathode more advantageous in boosting cathode performance.

Water-flooding in the cathode is the key factor limiting air-breathing the discharge performance of μDMFCs. There is a large amount of vapor generated in the electrochemical reaction, and a portion of it turns into the liquid state. It makes the air unable to access the gas diffusion layer, and decreases the reaction area, thereby degrading the cell performance. In this model, the water content was presented by liquid saturation. Fig. 7 shows the saturation distribution on the surface of the catalyst layer of the perforated and spoke cathode. The latter shows a lower content than the former, indicating a higher discharge capability. This is due to the spoke cathode's characteristics of high temperature and high pressure, which gives rise to a higher diffusion rate and evaporation. According to Fig. 7(b), the liquid saturation in the four right-angle areas is lower than the surrounding areas, and thus, water is more capable of being discharged in these areas. This provides a theoretical basis for further design of the water collection system in the cathode.

Fig. 8 shows the distributions of the oxygen concentration and temperature in the spoke cathodes with different numbers of blades, namely 2, 4 and 8. The blade widths are all 200 μm. The 8-blade configuration showed a slightly higher oxygen concentration distribution than the 4-blade did. Moreover, the distributions of the 4-blade and the 8-blade were relatively uniform, whereas there was a low mass transport area appearing in the 2-blade, which may give rise to concentration polarization. The average temperature of the cathode is enhanced with the increasing blades, but this variation was small. It is interesting to note that the 4-blade presented the most uniform distribution with a mere temperature difference of 0.0947 K, as shown in Fig. 8. The difference of the 8-blade was 0.1043 K, and that of the 2-blade was 0.1271 K. Based on the above analysis, we came to the conclusion that the oxidant concentration distribution determined the reaction speed on the catalyst layer surface. Additionally, the internal temperature affected the activity of the catalyst, the oxidant mass transport and the generated water. However, the oxidant was sufficient for a self-breathing DMFC with either 4 or 8 blades. Therefore, the 2-blade cathode was considered to have the worst performance, and there was no distinct performance difference between the 8-blade and the 4-blade.

3. Fabrication and assembly

In this work, the self-breathing μDMFC with the spoke cathode structure was fabricated by bulk-silicon MEMS technology [21]. It consisted of two plates (anode and cathode) as current collectors and a membrane electrode assembly (MEA) between them, in a sandwich structure. The cathodes introduced with the different structures and parameters were fabricated using bulk-silicon technology, as shown in Fig. 9(a), and with the microfabricated flow field, the distribution area played the role of transporting reactants to the diffusion layer of the MEA. To enhance the electronic conductivity, Au layers were sputtered on one side of the bipolar plates. The image of the spoke cathode shown in Fig. 9(b) reveals that there are some burrs existed after the fabrication process.

A piece of 5-layered MEA with the area of 0.64 cm^2 was employed in this silicon-based μDMFC, which was fabricated by the catalyst coated membrane (CCM) method. First, the hydrophilic catalyst layers were prepared using the decal transfer method to form the CCM, with an anode catalyst layer of Pt–Ru back (4.0 mg cm^{-2}), a cathode catalyst layer of Pt back (4.0 mg cm^{-2}) and a Nafion117 membrane between them. Afterwards, carbon paper (TGPH-090, Toray Inc.) was prepared with the hydrophobic (10 wt.% PTFE for the anode and 30 wt.% PTFE for the cathode) and pore-formed (NH_4HCO_3) pretreatment to form the gas diffusion layer (GDL). Finally, the 5-layered MEA was achieved with two GDLs hot pressed on both sides of the CCM at 130 °C and 4 MPa for 120 s. In addition, before operation, the MEA needed an activation process to achieve the optimal performance. First, to humidify the MEA, we fed 90 °C deionized water to the anode side and saturated oxygen (80 °C, ambient pressure) to the cathode side, and then we maintained the cell at 80 °C for 1 h. Second, to activate the catalysts, with the cell maintained at 80 °C, and we fed 2.0 M methanol solution with a flow rate of 5.0 mL min^{-1} to the anode and saturated oxygen at 720 mL min^{-1} to the cathode. Under these conditions, the cell was kept operating at 0.2 V for 4 h. Thus, the MEA was then completely activated.

In this work, a novel encapsulation approach was also designed using polydimethylsiloxane (PDMS), which could easily contact the silicon wafer with constriction. The fabrication process of the PDMS assembly is described in Fig. 10. A polymethyl methacrylate (PMMA) mold was first fabricated and cleaned, and then a PDMS elastomer and curing agent with a vacuumized weight ratio of 10:1 was poured into the face-to-face PMMA mold in a vacuum drying oven at 65 °C. After 90 min, the current collectors patterned with PDMS were molded. Finally, the holes and windows were created by laser cutting technology. Fig. 11(a) and (b) illustrate the schematic diagram of the assembled μDMFC and real feature, respectively.

4. Results and discussion

To analyze the impact of the cathode structure on the performance of the self-breathing μDMFCs, all the experiments were performed at a temperature of 20 °C and used the same anode flow field with the same configuration and geometry as the serpentine flow field and fed with 1.0 M methanol solution with the flow rate of 1.0 mL min^{-1} [22,23].

Fig. 12 shows the test results on the performance. The findings show that compared with the perforated cathode, while the contact area between the diffusion layer and the board was decreased in the spoke cathode, the open-circuit voltage and maximum power density were both effectively improved to 569.6 mV and 14.79 mW cm^{-2}, respectively. This indicates the feasibility and advantages of the spoke cathode. According to the simulation, the spoke cathode has the following advantages. (1) It weakened the phenomenon of methanol crossover and increased the open-circuit

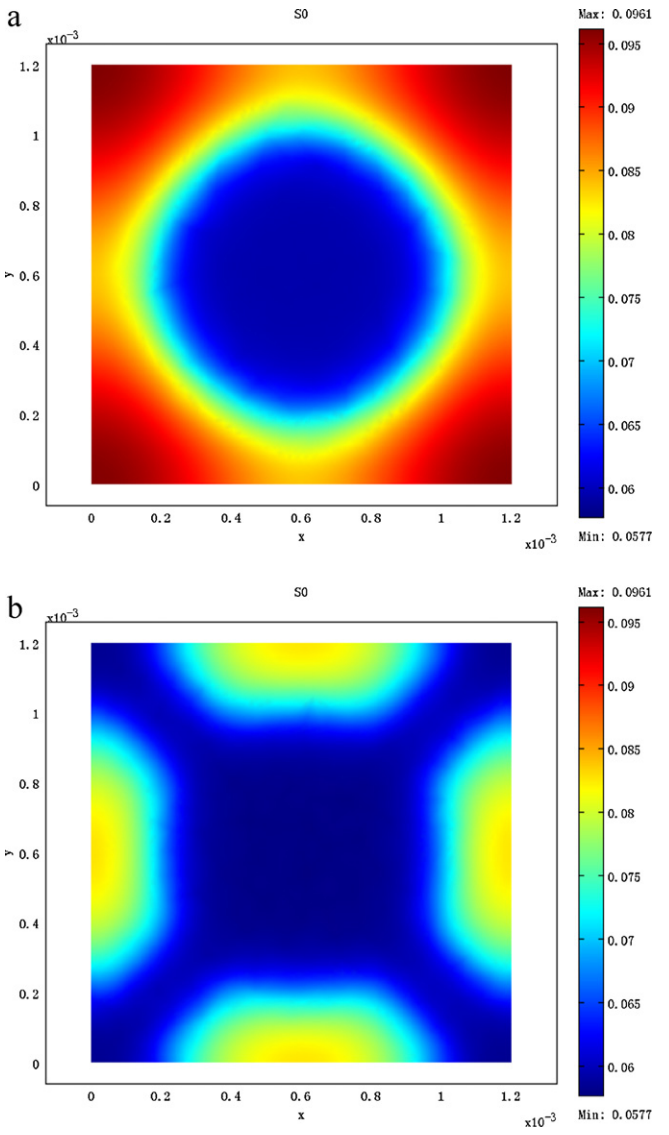

Fig. 7. Liquid saturation distributions at the catalyst layers with different cathode structures: (a) perforated cathode and (b) spoke cathode.

voltage. (2) Molecule mass transport rate was boosted, making the oxidant distribute uniformly. (3) The diffusion of water from the cathode to the PEM was promoted and decreased the inner resistance. (4) The operational temperature rose, thereby raising the catalyst reactivity and the water evaporation rate.

During the long-term operation of the air-breathing μDMFCs, a portion of the water generated in the cathode turns into the liquid state and stays on the surface of the catalyst layer. This prevents oxygen from joining the reaction. Meanwhile, the active area of the electrode declines, which gradually degrades the cell performance and leads to marked variations. Fig. 13 shows the test result of the transient performance at 30 mA cm^{-2} with a duration of 100 min (6000 s). As shown, there were obvious variations in the output of the perforated cathode, followed by a gradual decrease. The spoke cathode showed a relatively stable performance and improved capability for discharging water.

Fig. 14 shows the performance of the self-breathing μDMFCs with different numbers of blades. The outputs declined in the order of the 4-blade, the 8-blade and the 2-blade, and the maximum power densities were 14.79, 14.01 and 13.33 mW cm^{-2}, respectively. The test results indicated that the cell performance change with the number of blades was rather small. Additionally, there

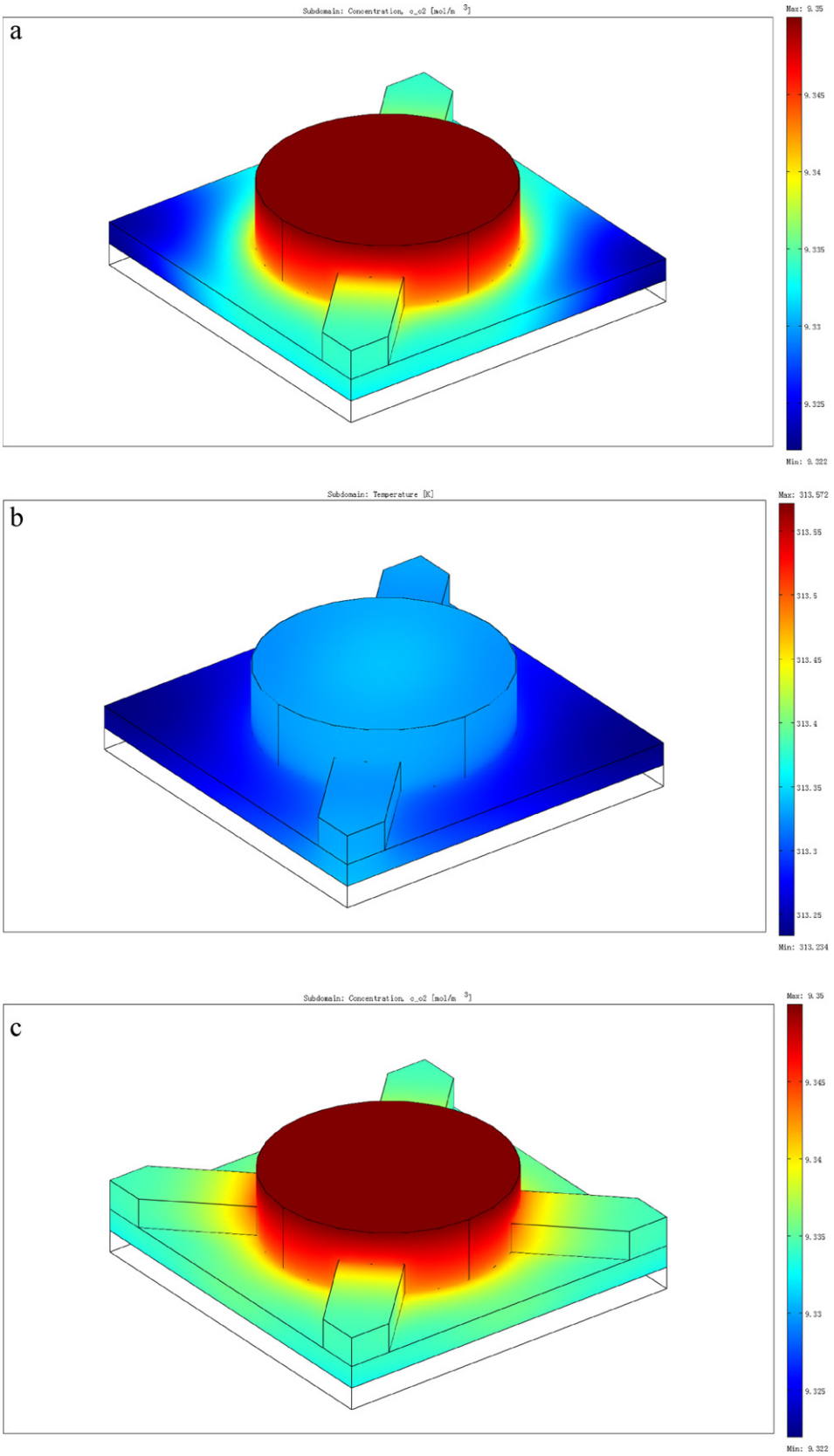

Fig. 8. Distributions of the oxygen concentration (mol m^{-3}) and temperature (K) in the spoke cathodes with different numbers of blades: (a) oxygen concentration distribution in the two-spoked cathode; (b) temperature distribution in the two-spoked cathode; (c) oxygen concentration distribution in the four-spoked cathode; (d) temperature distribution in the four-spoked cathode; (e) oxygen concentration distribution in the eight-spoked cathode; and (f) temperature distribution in the eight-spoked cathode.

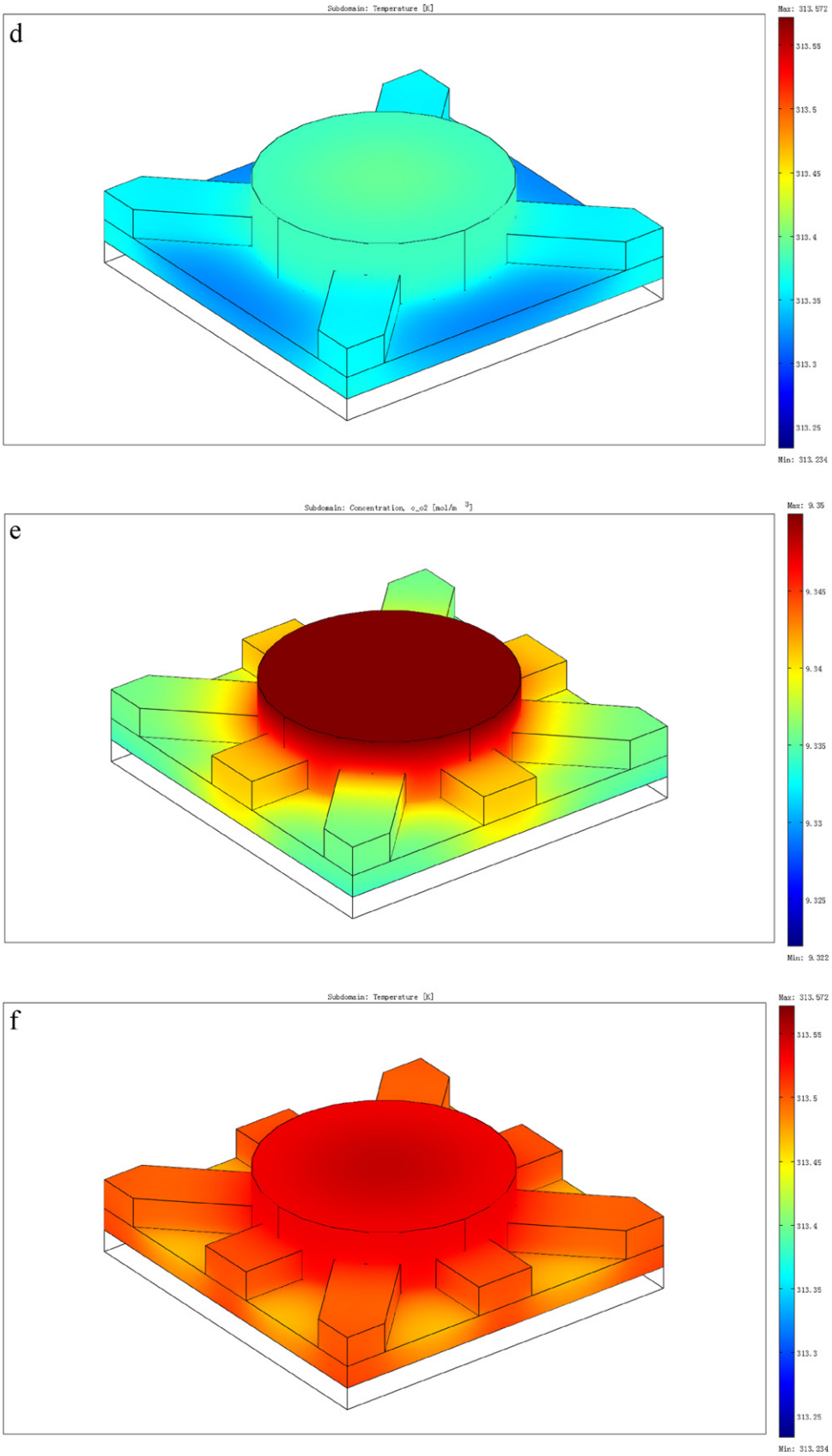

Fig. 8. continued.

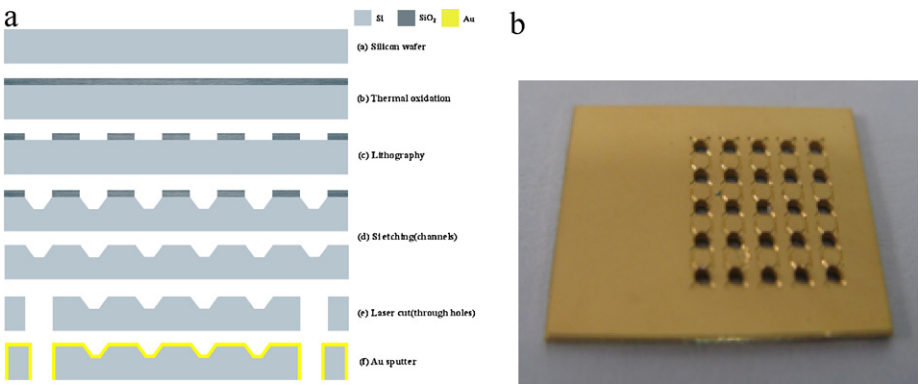

Fig. 9. (a) Schematic of the fabrication process of the silicon-based current collector and (b) photographs of spoke cathode.

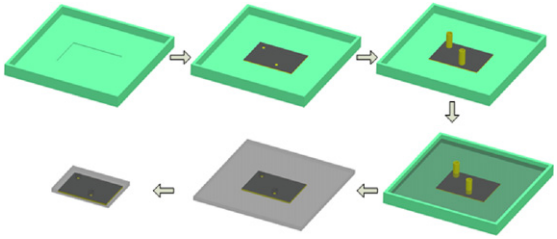

Fig. 10. Schematic of the assembly process using PDMS

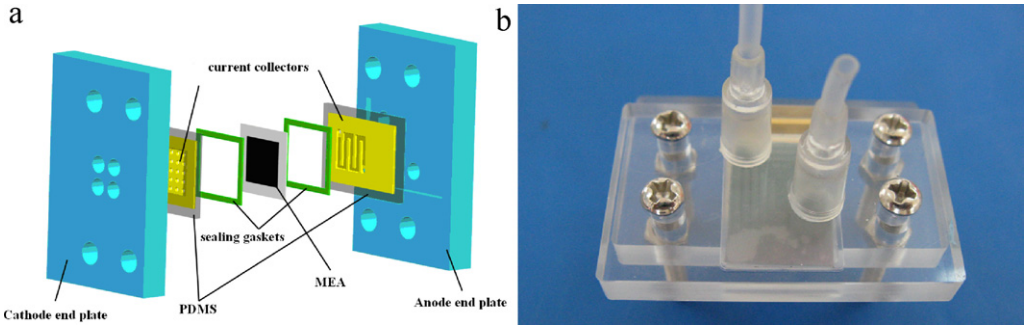

Fig. 11. The silicon-based μDMFC: (a) schematic of the silicon-based μDMFC structure; (b) real features of the assembled μDMFC.

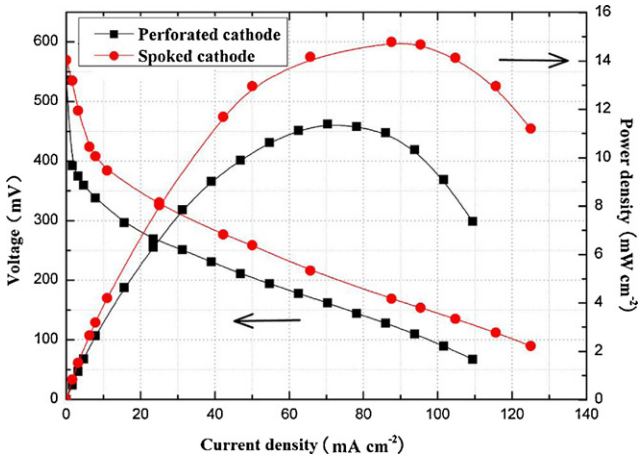

Fig. 12. Performance comparison of the air-breathing μDMFC with different cathode structure.

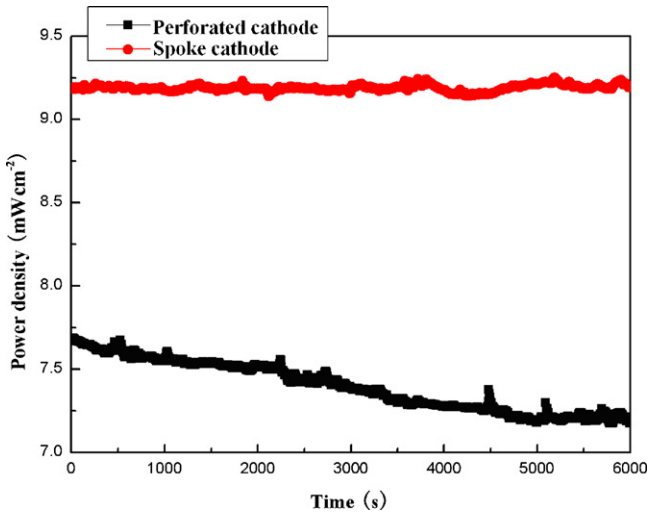

Fig. 13. Durability of the air-breathing μDMFC with different cathode structure.

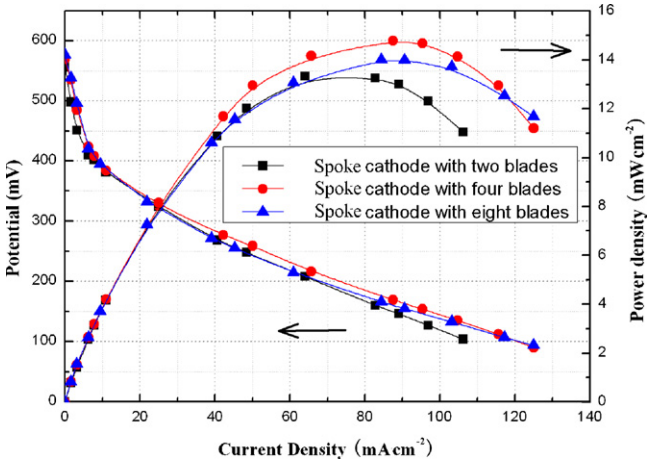

Fig. 14. Performance comparison of the air-breathing μDMFC with the spoke cathodes varying in the blade numbers.

was little difference in the results in Fig. 8, because some parameters used in our experiment may not be consistent with the model values of our cell. In comparison the 4-blade cathode, the 8-blade reduced more contact area between the diffusion layer and the current collector, leading to the increased contact resistance.

5. Conclusions

We designed and fabricated a silicon-based self-breathing μDMFC with a new spoke cathode structure using MEMS technology. To prove the superiority of the new cathode structure, a three-dimensional model that couples momentum transport, mass transports and heat transport with electrochemistry was developed and simulated. Compared with the conventional perorated cathode structure, the new one can improve the cell performance and water removal due to an increase in oxygen transport efficiency and pressure on the catalyst layer. The peak power density of the assembled μDMFC by the PDMS packaged was 14.79 mW cm^{-2} at room temperature using 1 M methanol solution at ambient pressure. Moreover, the stability tests of the self-breathing μDMFC demonstrated that the spoke structure can remove the water in the cathode effectively. From the results obtained in this work, it can be concluded that the self-breathing μDMFC with the new cathode structure could have potential advantages in the development of high power sources for portable electronic devices and MEMS.

Table 1
Physical and electrochemical kinetic parameters.

Nomenclature	
D_{O_2}	Diffusibility of oxygen 2.08×10^{-5} (m^2 s^{-1})
F	Faraday constant 96485 (C mol^{-1})
ΔG_c	Gibbs free energy -711.24×10^3 (J mol^{-1})
R	Gas law constant 8.314 (J mol^{-1} K^{-1})
ΔH_c	Reaction enthalpy -857.49×10^3 (J mol^{-1})
K	Permeability 1.2×10^{-12} (m^2)
M_{O_2}	Molar mass of oxygen 0.032 (kg mol^{-1})
M_{H_2O}	Molar mass of water 0.018 (kg mol^{-1})
M_{N_2}	Molar mass of nitrogen 0.014 (kg mol^{-1})
S_a	Specific ares 10^{-9} (m^{-1})
T_0	Working temperature 293 (K)
$c_{O_2,in}$	Oxygen concentration on the inlet 9.35 (mol m^{-3})
$c_{O_2,ref}$	Reference concentration of oxygen $2.1 \times P_{atm}/(RT_0)$
h_v	Latent heat of water 44.86×10^3 (J mol^{-1})
i_0	Reference exchanged current density on the cathode $0.04222 \exp\left(\frac{73200}{R}\left(\frac{1}{353}-\frac{1}{T}\right)\right)$
k	Thermal conductivity 1.6 (W m^{-1} K^{-1})
n_d	Electro-osmotic drag coefficient 2.5
P_{atm}	Atmospheric pressure 1.013×10^5 (Pa)
Greek alphabet	
α_c	Transfer coeficient on the cathode 0.8
ε	Porosity 0.6
σ_l	Conductivity of the free electrolyte 5 (S m^{-1})
$\sigma_{l,eff}$	electrolyte effective conductivity 1 (S m^{-1})
μ_l	Viscosity of liquid-phase 0.9×10^{-3} (kg m^{-1} s^{-1})
μ_g	Viscosity of gas-phase 14.96×10^{-6} (kg m^{-1} s^{-1})
ρ_g	Air density 1.29 (kg m^{-3})
ρ_{O_2}	Oxygen density 1.429 (kg m^{-3})
σ	Surface tension coeficient 0.625 (N m^{-1})
$\sigma_{s,eff}$	solid-phase effective electronic conductivity 1000 (S m^{-1})
ϕ_l	Overpotential for electrolyte 0.3 (V)
ϕ_s	Overpotential in catalyst layer 0.7 (V)
$w_{H_2O,in}$	Mass fraction of vapor on the inlet 0.001
$w_{N_2,in}$	Mass fraction of nitrogen on the inlet 0.766
$w_{O_2,in}$	Mass fraction of oxygen on the inlet 0.233

Acknowledgements

The work described in this paper was supported by the National Natural Science Funds of China (Nos. 60806037 and 61076105), a grant from the Ph.D. Programs Foundation of the Ministry of Education of China (No. 20102302110026), the Natural Scientific Research Innovation Foundation in Harbin Institute of Technology (HIT. NSRIF. 2009008) and Key Laboratory Opening Funding of Key Laboratory of Micro-Systems and Micro-Structures Manufacturing, Ministry of Education (HIT. KLOF. 2009003).

References

[1] S.K. Kamarudin, F. Achmad, W.R.W. Daud, Int. J. Hydrogen Energy 34 (2009) 6902.
[2] T. Pichonat, B. Gauthier-Manuel, Microsyst. Technol. 13 (2007) 1671.
[3] J.G. Liu, T.S. Zhao, R. Chen, et al., Electrochem. Commun. 7 (2005) 288.
[4] A. Kundu, J. Power Sources 170 (2007) 67.
[5] C.K. Dyer., J. Power Sources 106 (2002) 31.
[6] S.K. Kamarudin, W.R.W. Daud, S.L. Ho, et al., J. Power Sources 163 (2007) 743.
[7] H. Yang, T.S. Zhao, Q. Ye, J. Power Sources 142 (2005) 117.
[8] G.Q. Lu, C.Y. Wang, J. Power Sources 144 (2005) 141.
[9] H. Dai, H.M. Zhang, Q.T. Luo, et al., J. Power Sources 185 (2008) 19.
[10] N. Hashim, S.K. Kamarudin, W.R.W. Daud, Int. J. Hydrogen Energy 34 (2009) 8263.
[11] B. Zhang, Y.F. Zhang, H. He, et al., J. Power Sources 195 (2010) 7338.
[12] Q. Zhang, X.H. Wang, L.Y. Zhong, et al., Sens. Actuators A: Phys. 154 (2009) 247.
[13] C.W. Wong, T.S. Zhao, Q. Ye, et al., J. Power Sources 155 (2006) 291.
[14] S.H. Kim, H.Y. Cha, C.M. Miesse, et al., Int. J. Hydrogen Energy 34 (2009) 459.
[15] J.P. Esquivel, N. Sabaté, J. Santander, et al., J. Power Sources 194 (2009) 391.
[16] R. Chen, T.S. Zhao, W.W. Yang, C. Xu, J. Power Sources 175 (2008) 276.
[17] J.J. Hwang, S.D. Wu, J. Power Sources 161 (2006) 240.
[18] Z. Guo, A. Faghri, J. Power Sources 160 (2006) 1183.
[19] V.B. Oliveira, C.M. Rangel, A.M.F.R. Pinto, J. Chem. Eng. 157 (2010) 174.
[20] G.-B. Jung, A. Su, C.-H. Tu, Y.-T. Lin, F.-B. Weng, S.-H. Chan, J. Power Sources 171 (2007) 212.
[21] L. Zhong, X. Wang, Y. Jiang, et al., Sens. Actuators A 143 (2008) 70.
[22] A.A. Kulikovsky, Electrochem. Commun. 4 (2002) 939.
[23] K. Scott, W. Tama, J. Cruickshank, J. Appl. Electrochem. 28 (1998) 289.